Biosensors and Bioelectronics 152 (2020) 112012

Contents lists available at ScienceDirect

Biosensors and Bioelectronics

journal homepage: http://www.elsevier.com/locate/bios

Assembly of black phosphorus quantum dots-doped MOF and silver nanoclusters as a versatile enzyme-catalyzed biosensor for solution, flexible substrate and latent fingerprint visual detection of baicalin

Xiaowen Jiang [1], Hui Jin [1], Yujiao Sun, Zejun Sun, Rijun Gui [*]

College of Chemistry and Chemical Engineering, Intellectual Property Research Institute, Qingdao University, Shandong, 266071, PR China

ARTICLE INFO

Keywords:
Black phosphorus quantum dots
Silver nanoclusters
Baicalin
Visual detection
Latent fingerprint

ABSTRACT

In this work, a versatile enzyme-catalyzed biosensor was developed by using the assembled nanohybrids of black phosphorus quantum dots (BPQDs)-doped metal-organic frameworks (MOF) and silver nanoclusters (AgNCs). The nanohybrids of AgNCs/BPQDs/MOF exhibit dual-emissive fluorescence (FL) centers at 630 nm (red) and 535 nm (blue) under excitation at 440 nm. Baicalin enhances the activity of catalase and catalytic decomposition of H_2O_2. With increase of baicalin contents in the mixture containing nanohybrids, catalase and H_2O_2, the catalase-caused decomposition of H_2O_2 was accelerated and the excessive H_2O_2 was consumed. Baicalin can restrain the oxidation capability of H_2O_2. The red-FL (response signal) of AgNCs adhering to MOF increases, while blue-FL (reference signal) of BPQDs doped into MOF has negligible changes. A new ratiometric FL biosensor was designed based on nanohybrids and enzyme-catalyzed reaction. This biosensor enables the detection of baicalin in the range of 0.01–500 μg mL^{-1}, with a limit of detection of 3 ng mL^{-1}. This biosensor has high sensitivity, selectivity and stability for baicalin detection in practical samples. Especially, it performed the solution, flexible substrate and latent fingerprint visual detection of baicalin through direct observation of FL color shades with naked eyes. This work explored a facile and efficient semi-quantitative method for versatile FL visual detection, which can promote the development of advanced chemo/bio-sensors and analysis methods.

1. Introduction

As one kind of flavonoids extracted from *Scutellaria baicalensis*, baicalin (BAI) has biological activities, such as anti-bacteria, anti-inflammatory, anti-thrombosis, antiasthma, anticancer, hemostasis and detoxification (He et al., 2016; Sithisarn et al., 2019; Guo et al., 2019; Lee et al., 2015b; Li et al., 2019; Jin et al., 2019b; Xiao et al., 2019). When large doses of BAI injection preparations are used, adverse physiological reactions of human bodies may happen, especially low fever, muscle soreness, leukopenia, gastric discomfort, diarrhea and bullous drug eruption. Illegal addition of excessive BAI in medicines can cause human body damage. Hence, accurate detection of BAI is required and is conducive to the monitoring of drug security and human health. Traditional technologies were used to detect BAI, such as solid-phase extraction (Gu et al., 2015), high-performance liquid chromatography (HPLC) tandem mass spectrometry (MS) (Baygildieva et al., 2018), liquid chromatography (LC) tandem MS (Chung et al., 2012; Tong et al., 2012) and LC-ultraviolet absorption (Wei et al., 2016). These technologies undergo unavoidable problems, such as requirements of sophisticated pretreatments, well-trained technicians, time-consuming operations, laborious steps and low detection selectivity. To overcome the problems, it is required to develop facile, rapid and efficient methods for accurate detection of BAI. Chemo/bio-sensors have obvious advantages for target detection, such as convenient steps, high selectivity, sensitivity, stability and applicability. Electrochemical sensors were used to detect BAI through single-signal output mode (Zhang et al., 2016a; Hu et al., 2018a; Xie et al., 2017; Liu et al., 2014; Sheng et al., 2017). This mode depends on accurate measurements of signal intensities (Huang et al., 2018; Lee et al., 2015a; Wu et al., 2016; Jin et al., 2017; Gui et al., 2019; Fu et al., 2018b; Jiang et al., 2019). However, signal intensities are difficult to measure accurately due to possible effects of intrinsic and extrinsic factors, such as instrument errors, background signals and the fluctuation of environmental conditions.

As classic metal-organic frameworks (MOF), zeolitic imidazolate

* Corresponding author.
E-mail addresses: guirijun@163.com, guirijun@qdu.edu.cn (R. Gui).
[1] These authors have the equivalent contribution to this work.

https://doi.org/10.1016/j.bios.2020.112012
Received 28 October 2019; Received in revised form 6 January 2020; Accepted 7 January 2020
Available online 11 January 2020

frameworks (ZIF) have attracted much interest in recent years because of great application prospects in chemical separation, gas storage, drug delivery, catalysis and sensors (Bian et al., 2015; Lai, 2018; Zhong et al., 2018; Sun et al., 2019). ZIF has many fascinating properties, such as ultrahigh surface area, abundant functionality, highly ordered crystal microstructure, mechanical, thermal and chemical stability. Pure ZIF and its derivatives were used as multifunctional materials with superior properties and versatile applications (Bétard and Fischer, 2012). In previous studies, ZIF-8 often serves as a carrier vehicle for drug delivery (Ren et al., 2014). Scientists studied the modification of ZIF-8 with functional molecules, and explored its immobilization with biomolecules and nanomaterials for electronic and biomedical applications (Bian et al., 2015; Sun et al., 2019). To endow ZIF-8 with luminescence, various functional materials such as semiconductor quantum dots (QDs), graphene QDs, carbon dots, organic dyes, g-C_3N_4, metal nanoclusters and lanthanide luminous were combined with ZIF-8 through encapsulation, adsorption and core/shell assembly to develop the luminescent ZIF-8 composites for chemo/bio-detection and biomedicine. The ZIF-8 composite-based chemo/bio-sensors can be used for luminescence detection of metal ions, anions, contaminants, biomolecules, disease biomarkers, toxins, radicals, DNA and microRNA (Chen et al., 2015; Xu et al., 2016; Wang et al., 2017; Gao et al., 2017, 2018; Sammi et al., 2018; Ye et al., 2015; Liu et al., 2019b). Currently, visual detection based on luminescent ZIF-8 composites is still barely explored (Jalili et al., 2019; Fu et al., 2018a), which is of great importance in biomedical diagnose and clinical therapeutics.

Black phosphorus quantum dots (BPQDs, BP nanodots or nanoparticles) as the classic form of BP nanostructures are emerging functional nanomaterials (Gui et al., 2018). BPQDs can be prepared through liquid-phase exfoliation, mechanical breaking and thermal treatments of bulk BP crystals. Superior fluorescence (FL) properties of BPQDs have inspired the exploration of BPQDs-based sensors or devices in recent years (Gu et al., 2017a, 2017b; Lee et al., 2017; Long et al., 2018; Wang et al., 2018a; Ge et al., 2019; Yue et al., 2019). According to respective merits, the combination of BPQDs with MOF can form a hybrid complex with synergistic effects for applications. Previous studies mentioned the hybridization of MOF with two-dimensional (2D) BP for photocatalysis (Wang et al., 2016), direct anchoring of 2D NiCo-MOF on few-layer BP for advanced lithium-ion batteries (Jin et al., 2019a), and the engineering of BP to porous g-C_3N_4-MOF membrane with photocatalytic performance (Hu et al., 2019). Liu et al. reported the encapsulation of BPQDs into layered MOF (MIL-101-NH_2) to fabricate a tandem catalyst for enhanced therapy against hypoxic tumor cells (Liu et al., 2019a). Prior studies hardly involved the hybridization of BPQDs with MOF and functional modification of BPQDs/MOF hybrid. To expand applications, we developed new BPQDs/MOF complex. Different from 2D BP/MOF and BPQDs/MOF hybrid used for photocatalysis, batteries and photodynamic therapy, the new complex was explored towards efficient visual analysis methods and was used as a versatile biosensor for naked-eye visual FL detection of targets.

Herein, we reported a novel dual-signal ratiometric FL method for BAI detection. Dual-signal output mode has an intrinsic built-in correction of signal intensities, which can restrain the effects of interference factors and endow with high detection accuracy (Huang et al., 2018; Lee et al., 2015a). In this work, a versatile dual-signal ratiometric FL biosensor of BAI was explored based on enzyme-catalyzed reaction. ZIF-8 with doping of BPQDs was prepared by solvothermal reaction, followed by assembly with silver nanoclusters (AgNCs) to produce AgNCs/BPQDs/MOF nanohybrids. In aqueous suspension of nanohybrids containing catalase and H_2O_2, the addition of BAI enhances catalase activity and facilitates the catalytic decomposition of H_2O_2 by catalase. BAI restrains oxidation capability of H_2O_2. The red-FL (630 nm) of AgNCs increases. BPQDs doped into MOF have negligible changes of blue-FL (reference signal, 535 nm). By plotting a linear relationship between $\mathbf{I}_{BPQDs}/\mathbf{I}_{AgNCs}$ ($\mathbf{I}_{535}/\mathbf{I}_{630}$) and BAI concentration ($\boldsymbol{C}_{BAI}$), a novel ratiometric FL biosensor of BAI was constructed (Scheme 1). The biosensor was used for efficient detection of BAI in practical samples, with high detection performances. It realized the solution, flexible substrate and latent fingerprint visual detection of BAI through observing naked-eye visual FL color shades.

2. Experimental section

This section includes the contents of instruments and all experimental procedures (Gu et al., 2017a; Ren et al., 2018). The detailed contents are available in Electronic Supplementary Material (ESM).

3. Results and discussion

3.1. Morphology, microstructure and property characterizations

The morphologies and microstructures of the products were characterized by TEM images. The prepared BPQDs show nearly dispersible nanoparticles (NPs) with an average diameter of ~4.5 nm (Fig. 1a). The inserted HR–TEM images give lattice fringes of 0.33 nm and 0.51 nm, which are respectively attributed to the (021) and (020) planes of BP crystals (Zhang et al., 2015). Fig. 1b exhibits the almost uniform NPs of AgNCs with a narrow diameter distribution of 10–15 nm and a mean diameter of ~12.8 nm (Jiang et al., 2019). In Fig. 1c, ZIF-8 MOF complex with doping of BPQDs displays dispersible NPs that have typical hexagonal morphologies of ZIF-8 (Sun et al., 2019). BPQDs with smaller sizes were doped into larger-sized ZIF-8 (0.25–0.56 μm). They are hardly observable in ZIF-8 even if using local amplification (Fig. 1d). After coupling of AgNCs with ZIF-8 complex, the assembled AgNCs/BPQDs/MOF nanohybrids display typical hexagonal morphologies of ZIF-8 (Fig. 1e) and partial NPs (few tens of "nm" in size) around ZIF-8 through local amplification of TEM images (Fig. 1f). According to preparation principles and experimental results, partial NPs are assigned to AgNCs. The results suggest successful preparation of the nanohybrids (Hu et al., 2018b).

XRD patterns of products were characterized in Fig. 2a. MOF shows a group of sharp diffraction peaks that are in accordance with stimulated XRD patterns of ZIF-8 crystals (CCDC no.602542) (Wang et al., 2018b). Compared with ZIF-8, the nanohybrids exhibit similar diffraction peaks of XRD patterns. The results reveal that the doping of BPQDs into ZIF-8 and the assembly of AgNCs with ZIF-8 during the preparation of nanohybrids hardly influence the crystalline integrity of ZIF-8 (Sun et al., 2019; Ma et al., 2017; Wang et al., 2017). In FT–IR spectra (Fig. 2b), a characteristic band at 1402 cm^{-1} is assigned to C–H bending vibration. A band appears at 2930 cm^{-1} is due to C–H stretching vibration. Other labelled characteristic bands have similarities of C–C, C–O and C═C bonds from MOF, AgNCs and nanohybrids. The results demonstrate the combination of AgNCs with MOF in nanohybrids (Hu et al., 2018b). In Fig. 2c, the full-scan XPS spectra exhibit a group of characteristic peaks that indicate surface elements of P2p, C1s, Ag3d, O1s and Zn2p. The high-resolution XPS spectra suggest clear features of binding energies. Two distinct peaks at 129.7 and 130.5 eV in P2p are attributed to 2p3/2 and 2p1/2 orbitals of zero-valent phosphorous (P^0), respectively (Fig. 2d). A broad peak at 132.8 eV comes from oxidized phosphorus (P_xO_y, P^{5+}), implying partial oxidization of P^0 during preparation and purification. The surface of BP nanostructures is sensitive to oxygen and moisture (Gui et al., 2018). Two distinct peaks at 368.3 and 374.2 eV are assigned to Ag^+ and Ag^0 states (Fig. 2e). The results suggest partial oxidization of Ag^0 to Ag^+ on the surface of nanohybrids.

Raman spectra were used to characterize BPQDs. In Fig. 2f, three prominent peaks demonstrate one out-of-plane photon mode (A^1_g) at 361.6 cm^{-1}, and two in-plane modes (B_{2g}, A^2_g) at 437.5 and 464.1 cm^{-1}. Compared with bulk BP crystals, B_{2g} and A^2_g modes of BPQDs show respective red shifts by 7.5 and 8.4 cm–1 A^1_g mode is red-shifted by 5.1 cm^{-1}. The frequency difference between A^1_g and B_{2g} modes shows a change from 75.1 cm^{-1} for bulk BP to 79.6 cm^{-1} for BPQDs (Zhang et al., 2015). These red-shifted properties are similar to the mode changes of

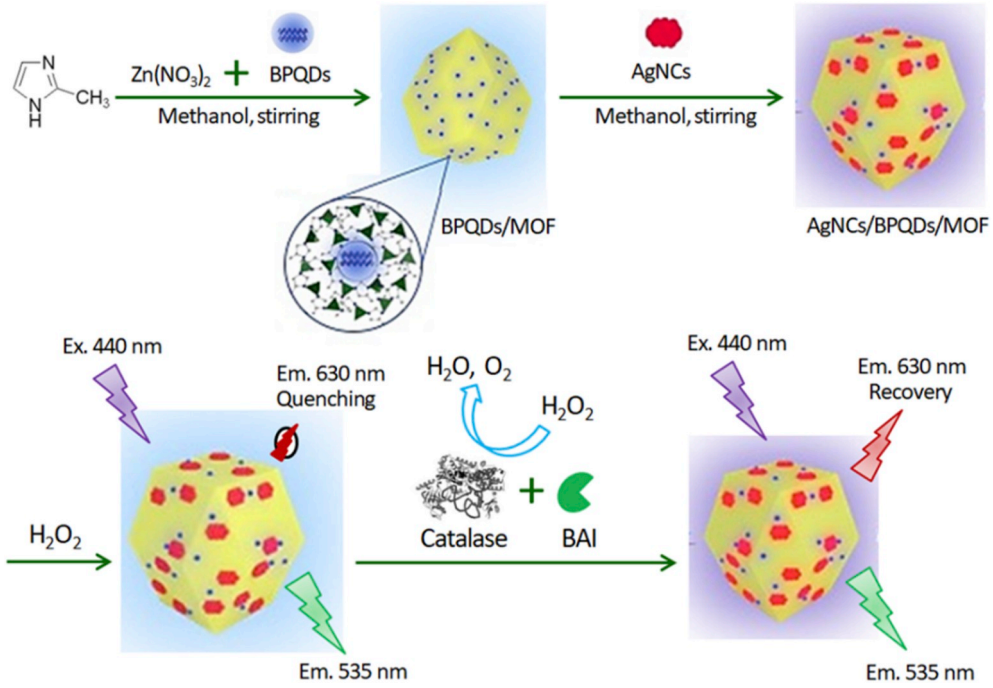

Scheme 1. Diagram of the construction process and application of AgNCs/BPQDs/MOF nanohybrids as a ratiometric FL biosensor for visual detection of BAI.

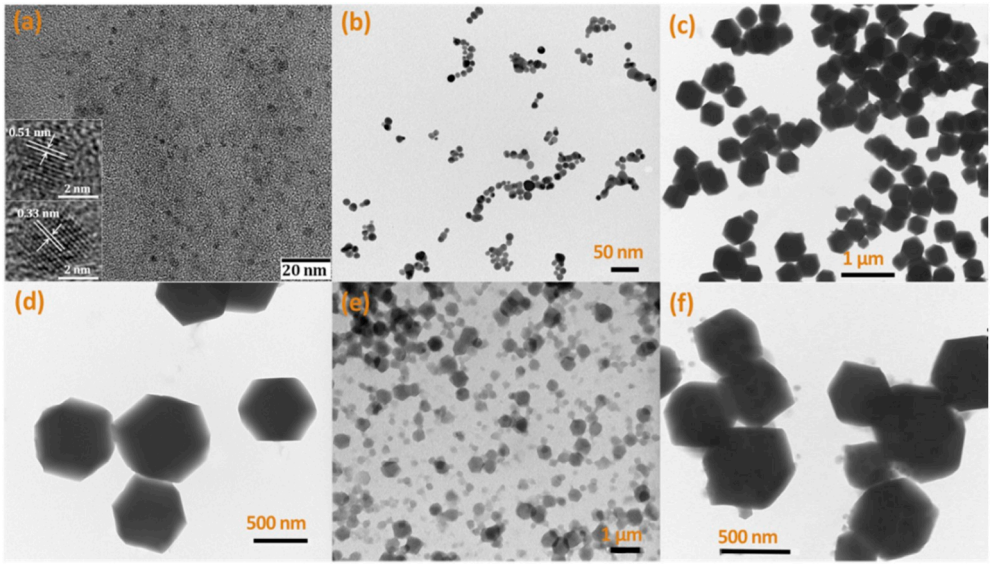

Fig. 1. TEM images of BPQDs (a), AgNCs (b), BPQDs-doped MOF before (c) and after (d) local amplification, AgNCs/BPQDs/MOF nanohybrids before (e) and after (f) local amplification. Insets show HR-TEM images of BPQDs (a).

MoS_2, boron nitride and graphene QDs with thin thicknesses and small dimensions (Lin et al., 2014; Stengl and Henych, 2013; Li et al., 2011). The similar Raman spectra indicate the microstructure of BPQDs derived from bulk BP. Fig. 2g characterizes N_2 adsorption–desorption isotherms. As for desorption branches, hysteresis loops gradually move to higher relative pressure, suggesting the coexistence of micropore and mesopore structures (Sun et al., 2019). The Brunauer-Emmett-Teller pore surface area and pore size (Fig. 2h) of nanohybrids are slightly smaller than that of MOF, revealing the impacts from BPQDs doping and AgNCs coupling on the pore surface area and size of MOF. Average Zeta potentials of BPQDs, AgNCs, MOF and nanohybrids were −11.13, −26.13, +27.66 and + 19.94 mV, respectively (Fig. 2i). BPQDs and AgNCs are negatively charged. A reduced Zeta positive potential of nanohybrids is attributable to the combination of BPQDs and AgNCs with MOF. Finally, the positively charged MOF dominates the Zeta potential of nanohybrids (Fu et al., 2018b).

3.2. UV–vis absorption spectra and FL spectra characterizations

Optical properties were studied by UV–vis absorption and FL spectra. Fig. 3a has a sharp absorption peak at 295 nm, originating from the features of BPQDs (Gui et al., 2018; Zhang et al., 2015). AgNCs have two characteristic absorption bands centered at 355 nm and 455 nm (Jiang et al., 2019; Ren et al., 2018; Xiong et al., 2016). UV–vis absorption spectra of nanohybrids exhibit the combined features of BPQDs and AgNCs. FL excitation spectrum of BPQDs displays a broad excitation

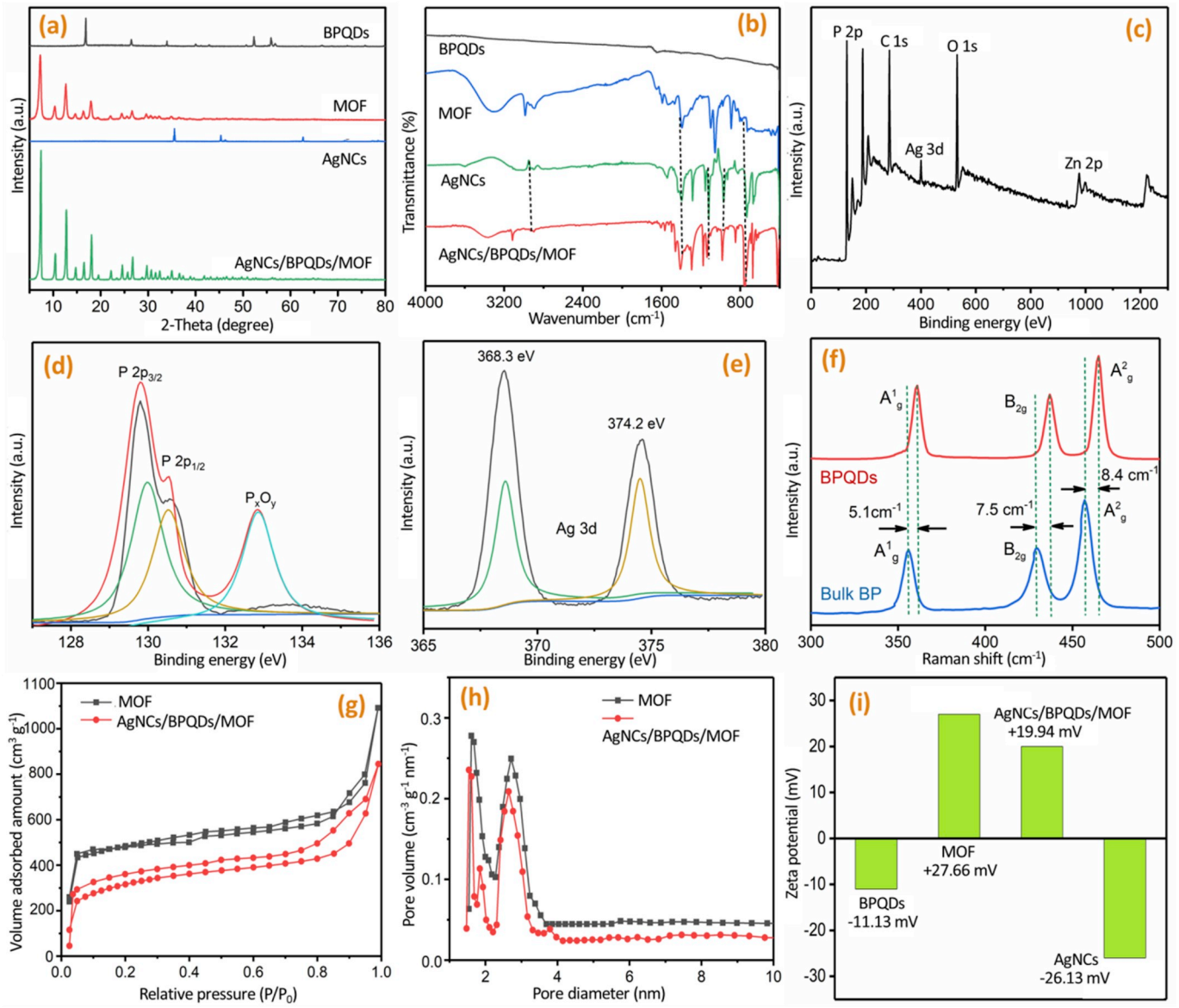

Fig. 2. XRD patterns (a) and FT–IR spectra (b) of BPQDs, MOF, AgNCs and AgNCs/BPQDs/MOF nanohybrids. (c) The full-scan XPS spectra of nanohybrids. The high-resolution XPS spectra of P2p (d) and Ag3d (e). (f) Raman spectra of BPQDs and bulk BP crystals. The N_2 adsorption–desorption isotherms (g) and pore diameter distributions (h) of MOF and nanohybrids. (i) Average Zeta potentials of BPQDs, MOF, AgNCs and nanohybrids.

region of 395–480 nm (Fig. 3b). The maximal excitation wavelength is 440 nm. FL emission spectra show respective emission peaks centered at 535 nm for BPQDs and 630 nm for AgNCs. The nanohybrids have dual-emissive FL peaks due to combination of BPQDs and AgNCs with MOF. The combination endows nanohybrids with dual-emissive features. Under excitation with a 365 nm UV lamp, aqueous dispersions of BPQDs, AgNCs and nanohybrids in cuvettes respectively show light-blue, deep-red and deep-blue visual FL colors (insets in Fig. 3b). Clear FL color shades between light-blue BPQDs and deep-red AgNCs can be distinguished by naked eyes conveniently. As for dual-emissive nanohybrids, when the target specially causes regular decrease of FL (AgNCs) and slight FL changes (BPQDs), FL color types (shades) vary from deep-red to deep-blue FL, including transition colors between two neighboring colors. The phenomenon is conducive to the development of naked-eye visual FL analysis methods (Fu et al., 2018b; Jiang et al., 2019).

3.3. Optimization of experimental conditions for FL measurements

To study optimal conditions for FL measurements, FL emission spectra of products were measured under various conditions, including salt concentration, pH and incubation time (Fig. S1). With increase of NaCl concentration (C_{NaCl}) from 0 to 0.5 M, FL peak intensities of AgNCs and BPQDs decrease gradually, showing salt-sensitive FL features. In the presence of 5 mM NaCl, 98% and 87% of FL emissions are retained. At the optimal concentration, buffer solutions were prepared to dilute or dissolve chemicals, biological reagents, products and practical samples. By extending incubation time from 0 to 60 min, FL peak intensities of AgNCs and BPQDs show reduced changes. After incubation for 5 min, more than 91% and 92% of FL emissions are maintained. The results confirm that the optimal incubation time prior to FL measurements is 5 min. As for AgNCs/BPQDs/MOF nanohybrids, FL spectra were measured under various conditions (Fig. S2). With increase of incubation time from 0 to 100 h, FL intensities at 630 nm (AgNCs) and 535 nm (BPQDs) reduce gradually. When incubation time reaches up to 100 h, more than 85% and 74% of FL emissions are retained. The results indicate high FL

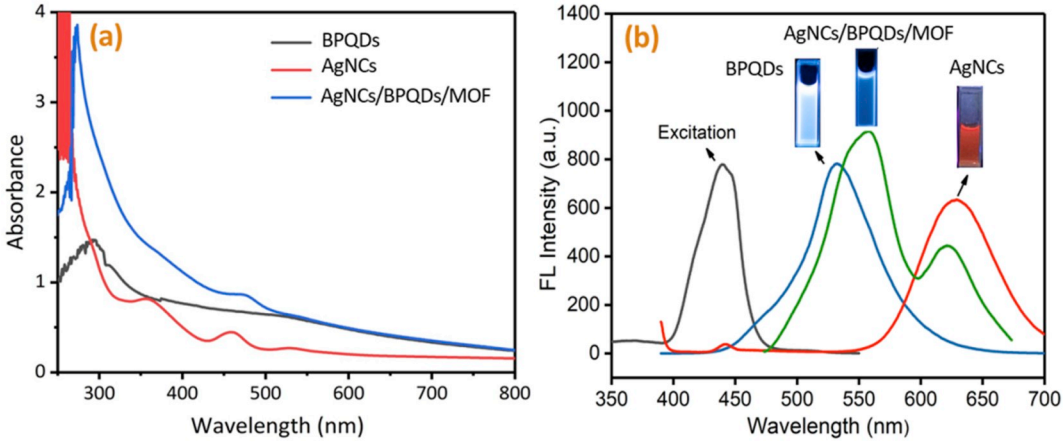

Fig. 3. UV–vis adsorption spectra (a), FL excitation and emission spectra (b) of BPQDs, AgNCs and AgNCs/BPQDs/MOF. Insets in (b) show FL color photographs collected from aqueous dispersions of products under excitation with a 365 nm UV lamp. (For interpretation of the references to color in this figure legend, the reader is referred to the Web version of this article).

stability of nanohybrids. Compared to FL emissions of AgNCs and BPQDs incubated for different times, the high FL stability of nanohybrids is attributed to the doping of BPQDs into MOF and the coupling (assembly) of AgNCs with MOF. By using a capping (stabilizer) carrier, MOF can promote FL stability of loaded fluorescent materials (Hu et al., 2018b; Feng et al., 2018). Besides, the nanohybrids exhibit high FL stability against $\boldsymbol{C}_{NaCl}$ varying from 0 to 0.5 M. BPQDs were doped into MOF and FL intensities at 535 nm present negligible effects on extrinsic pH conditions. AgNCs were assembled by coupling with MOF. Partial AgNCs contacted around the surface of MOF and thus responded to pH changes. AgNCs exhibit pH-responsive FL emissions because of protonation and deprotonation of lipoic acid as the surface stabilizing agent (Hu et al., 2018b). The maximal emission was achieved at pH 7.0, indicating the optimal pH for FL measurements of dual-emissive nanohybrids.

3.4. Construction and performance of ratiometric FL biosensor of BAI

FL spectra were measured under optimal conditions. With the increment of H_2O_2 concentration ($\boldsymbol{C}_{H2O2}$) from 0 to 110 μM, FL of AgNCs is reduced gradually (Fig. 4a). The quenching phenomenon originates from H_2O_2-triggered oxidation of central Ag^0 to Ag^+. A standard electrode potential of H_2O_2/H_2O (1.77 V) is much higher than Ag^+/Ag (0.799 V), and thus Ag^0 is easily oxidized to Ag^+ by H_2O_2 (Hu et al., 2018b). There is a well (R^2 = 0.9923) plotted linear relationship between relative FL intensities of AgNCs ($\mathbf{I}_0$–$\mathbf{I}/\mathbf{I}_0$) and $\boldsymbol{C}_{H2O2}$ (Fig. 4b). The results indicate that AgNCs enable efficient FL sensing of H_2O_2. After assembly of AgNCs with BPQDs-doped MOF, FL spectra of the nanohybrids were measured in the presence of H_2O_2. FL peak at 630 nm (AgNCs) shows regular decrease, while that at 535 nm (BPQDs doped in MOF) hardly changes (Fig. 4c). The results are accordance with previous studies (Hu et al., 2018b; Feng et al., 2018). There is a well (R^2 = 0.9976) linear relationship between relative FL intensities of nanohybrids ($\mathbf{I}_{535}/\mathbf{I}_{630}$) and $\boldsymbol{C}_{H2O2}$ (Fig. 4d). These results reveal that the nanohybrids can be used for ratiometric FL sensing of H_2O_2. BAI improves antioxidant activity of catalase and catalytic decomposition of H_2O_2. With the increase of $\boldsymbol{C}_{BAI}$ in the mixture containing nanohybrids, catalase and H_2O_2, the catalase-triggered decomposition of H_2O_2 was accelerated and excessive H_2O_2 was consumed. Besides, BAI restrains the oxidation capability of H_2O_2 (Meng et al., 2019; Kim et al., 2012; Wang, 2010; Zhang et al., 2016b; Shen et al., 2019; Wu et al., 2018). In the mixture of nanohybrids, catalase and H_2O_2, the addition of BAI induces remarkable changes of FL at 630 nm and slight changes of FL at 535 nm (Fig. 4e). Under excitation at 440 nm, red-FL (response signal) of AgNCs around MOF recovers due to H_2O_2 catalytic decomposition. BPQDs were doped into MOF and their blue-FL (reference signal) has slight responses on H_2O_2. There is a well (R^2 = 0.9935) plotted linear relationship between ratiometric FL ($\mathbf{I}_{535}/\mathbf{I}_{630}$) and $\boldsymbol{C}_{BAI}$ in the range of 0.01–500 μg mL^{-1} (Fig. 4f). Limit of detection (LOD) is ~3 ng mL^{-1}, calculated by signal-to-noise (S/N = 3). Therefore, a novel ratiometric FL biosensor of BAI was constructed by the nanohybrids based on enzyme-catalyzed reaction.

Previous studies reported different methods for BAI detection (Gu et al., 2015; Baygildieva et al., 2018; Chung et al., 2012; Tong et al., 2012; Wei et al., 2016; Zhang et al., 2016a; Hu et al., 2018a; Xie et al., 2017; Liu et al., 2014; Sheng et al., 2017), as summarized in Table S1. These methods utilized a single-signal output mode to detect BAI. The mode depends on accurate measurements of signal intensities, which are difficult to implement because of possible effects of intrinsic and extrinsic factors. To conquer the limitation, we explored a ratiometric dual-signal FL method to detect BAI. Ratiometric dual-signal output with an intrinsic built-in correction restrains the effects of interference factors and shows high detection accuracy (Huang et al., 2018; Lee et al., 2015a). Prior to this work, there is still no work involving ratiometric dual-signal output to detect BAI. To evaluate selectivity and sensitivity of the ratiometric FL biosensor, some ions and biomolecules were chosen as potential interferents (competitors) of BAI. With addition of interferents and BAI into the sensor system, FL emission spectra of mixture solutions were measured and $\mathbf{I}_{535}/\mathbf{I}_{630}$ values were calculated (Fig. 5a). Interferents (1 mM of ions, 3 mg mL^{-1} of biomolecules) cause slight (<0.07) changes of $\mathbf{I}_{535}/\mathbf{I}_{630}$. The addition of H_2O_2 (0.1 mM) or BAI (0.3 mg mL^{-1}) results in dramatic increase (0.59) or decrease (0.77) changes of $\mathbf{I}_{535}/\mathbf{I}_{630}$. The addition of "$H_2O_2$ *plus* all ions (9 mM)" or "BAI *plus* all biomolecules (27 mg mL^{-1})" leads to $\mathbf{I}_{535}/\mathbf{I}_{630}$ changes (0.60, 0.81), which are close to additions of H_2O_2 and BAI. Each interferent and the mixture of interferents with 10- or 90-fold higher coexisting concentration than BAI do not cause obvious influences on $\mathbf{I}_{535}/\mathbf{I}_{630}$. As testified (Fig. S3), the biosensor has selective and sensitive ratiometric FL responses on BAI over interferents and other flavonoids (Wang et al., 2013). The results indicate excellent accuracy, feasibility and practicability of the biosensor during BAI detection.

3.5. BAI detection in practical samples and versatile visual detection

To assess practicability of the biosensor in practical samples, the aqueous dispersions of BAI tablets without and with addition of BAI were detected by measuring FL spectra of mixture solutions. By using a linear relationship of $\mathbf{I}_{535}/\mathbf{I}_{630}$ *versus* $\boldsymbol{C}_{BAI}$ in Fig. 4f, $\boldsymbol{C}_{BAI}$ of samples was detected. In Table S2, the detected values of $\boldsymbol{C}_{BAI}$ are very close to the specified ones in BAI tablets. After addition of BAI in aqueous dispersions of BAI tablets, the detected $\boldsymbol{C}_{BAI}$ is in well agreement with spiked

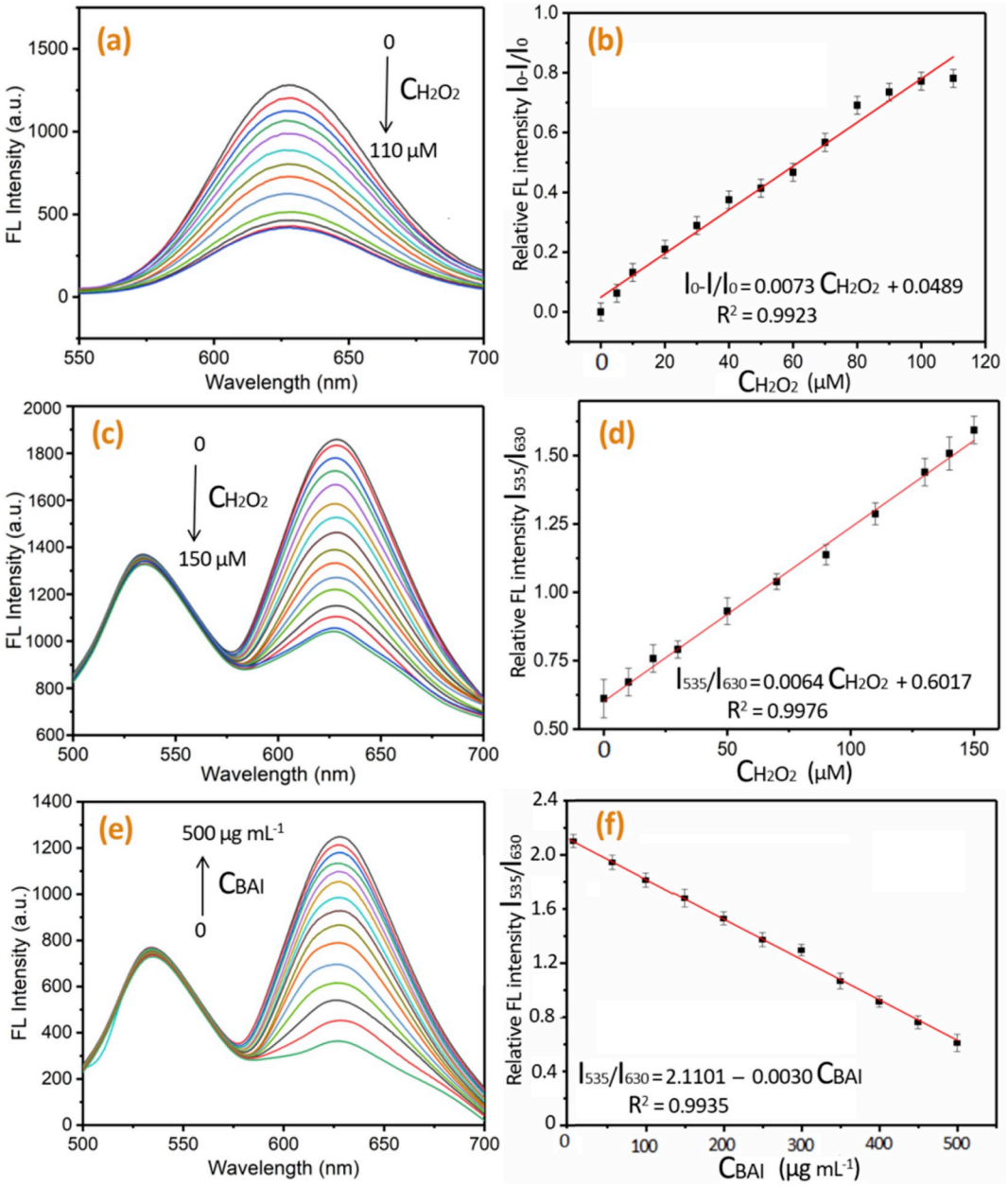

Fig. 4. FL spectra of AgNCs (a) and AgNCs/BPQDs/MOF nanohybrids (c) in the presence of H_2O_2. (e) FL spectra of nanohybrids in the presence of catalase (5 mU L^{-1}), H_2O_2 (150 μM) and BAI (0–500 μg mL^{-1}). (b) The plotted linear relationship between relative FL of AgNCs ($\mathbf{I_0}$–$\mathbf{I}/\mathbf{I_0}$, $\mathbf{I_0}$ and $\mathbf{I}$ stand for FL peak intensities before and after addition of H_2O_2) and $\boldsymbol{C}_{H2O2}$ based on curves in (a). (d) The plotted linear relationship between relative FL of the nanohybrids ($\mathbf{I_{535}}/\mathbf{I_{630}}$) and $\boldsymbol{C}_{H2O2}$ based on curves in (c). (f) The plotted linear relationship between $\mathbf{I_{535}}/\mathbf{I_{630}}$ and $\boldsymbol{C}_{BAI}$ based on curves in (e).

one, showing high detection recoveries of 96.0–104.6% and low relative standard deviations (RSD, $n = 6$) of 1.2–3.8%. The results confirm high practicability of the biosensor for efficient detection of BAI in practical samples. Versatile FL visual detection applications of the biosensor were investigated. BAI was externally added into aqueous dispersions of the sensor system. Ultimate $\boldsymbol{C}_{BAI}$ was adjusted from 0 to 500 mg mL^{-1}. BAI-containing mixture solutions were placed in cuvettes, or were directly dropped on flexible polyamide thin-film substrates and latent fingerprints. Under excitation with a 365 nm UV lamp, naked-eye visual FL colors were seen and were recorded by using a smartphone (Fig. 5b). Moreover, $\boldsymbol{C}_{BAI}$ in practical human serum samples without and with addition of BAI was detected by the plotted linear relationship. Detected values of $\boldsymbol{C}_{BAI}$ are in well agreement with spiked ones, accompanied by high detection recoveries and low RSD (Table S3). Under excitation with a 365 nm UV lamp, visual FL colors were collected from the sample-sensor mixtures dropped on flexible thin-films with latent fingerprints. We recoded the observable latent fingerprint photographs of FL imaging with a smartphone (Fig. S4). Visual FL latent fingerprint colors are in well agreement with that in Fig. 5b. Different visual FL colors reflect the specified values of $\boldsymbol{C}_{BAI}$ in respective samples. $\boldsymbol{C}_{BAI}$ was conveniently detected by versatile visual analysis. This work developed a novel analysis method for three-in-one (solution, flexible substrate, latent fingerprint) FL visual detection. The semi-quantitative method can be extended to other chemo/bio-sensors or devices, promoting further development of current visual analysis methods.

4. Conclusions

In summary, we constructed a novel and versatile ratiometric FL biosensor based on the assembled nanohybrids of AgNCs/BPQDs/MOF

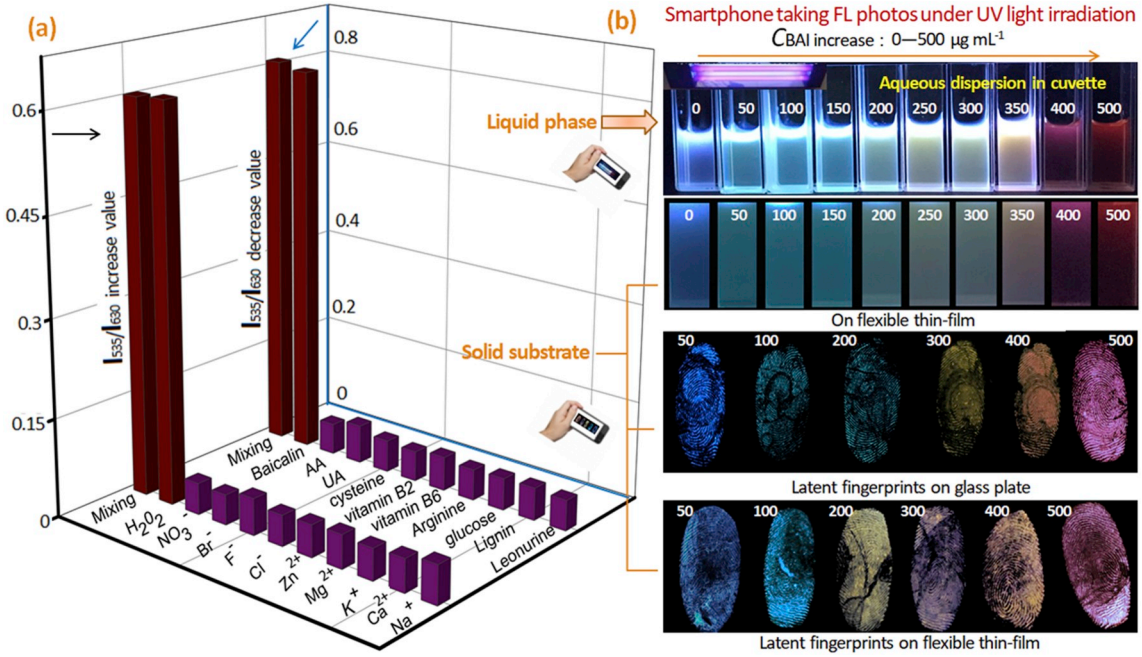

Fig. 5. (a) I_{535}/I_{630} increase and decrease values of the nanohybrids *plus* catalase with the addition of BAI, H_2O_2 and other interferents. In front columns, the mixing system of "nanohybrids *plus* catalase" contains all ions (9 mM) and H_2O_2 (0.1 mM). In rear columns, the mixing system of "nanohybrids *plus* catalase *plus* H_2O_2" contains all biomolecules (27 mg mL^{-1}) and BAI (0.3 mg mL^{-1}). (b) Aqueous dispersions of "nanohybrids *plus* catalase *plus* H_2O_2" with the addition of BAI (0–500 μg mL^{-1}) placed into cuvettes or dropped onto flexible thin-film substrates and latent fingerprints, excited with a UV lamp at 365 nm. Naked-eye visual FL color photographs were recorded on a commercial smartphone. (For interpretation of the references to color in this figure legend, the reader is referred to the Web version of this article).

and enzyme-catalyzed reaction. BPQDs-doped MOF complex was synthesized by one-pot solvothermal reaction. The nanohybrids were prepared through assembly of AgNCs with the complex. The aqueous dispersion of "nanohybrids *plus* catalase *plus* H_2O_2" served as the sensor system. Morphologies, microstructures and properties of products were characterized systematically. Various experimental conditions were optimized and detection mechanisms for BAI and H_2O_2 were discussed through measuring FL emission spectra. Under optimal conditions, there is a well-plotted linear relationship between the ratiometric FL (I_{535}/I_{630}) of the sensor system and C_{BAI} in the range of 0.01–500 μg mL^{-1}, with a low LOD of 3 ng mL^{-1}. The resultant biosensor has highly sensitive and selective ratiometric FL responses on BAI, against potential interferents. In practical BAI tablets, the biosensor enables efficient detection of BAI, with high detection recoveries and low RSD. Moreover, the biosensor realized versatile FL visual detection of BAI through placing BAI-containing mixture solutions in cuvettes or dropping on flexible thin-film substrates and latent fingerprints. C_{BAI} in samples can be indicated by directly observing visual FL color types (shades) by naked eyes. The developed biosensor enables rapid detection of BAI and the total assay time of BAI in samples is about 5 min. This work originally explored a novel analysis method for three-in-one FL naked-eye visual detection by smartphone. The practicable semi-quantitative analysis method can be extended to visual detection applications of other chemo/bio-sensors and devices, promoting the further development of current analysis methods.

Declaration of competing interest

The authors declare that they have no known competing financial interests or personal relationships that could have appeared to influence the work reported in this paper.

CRediT authorship contribution statement

Xiaowen Jiang: Writing - original draft. **Hui Jin:** Writing - original draft. **Yujiao Sun:** Investigation, Methodology. **Zejun Sun:** Investigation, Methodology. **Rijun Gui:** Conceptualization, Project administration, Supervision.

Acknowledgements

This work was financially supported by the Natural Science Foundation of Shandong Province, China (ZR2019MB026) and the Source Innovation Plan Application Basic Research Project of Qingdao, China (18-2-2-26 jch, 17-1-1-72-jch).

Appendix A. Supplementary data

Supplementary data to this article can be found online at https://doi.org/10.1016/j.bios.2020.112012.

References

Baygildieva, D.I., Baygildiev, T.M., Stavrianidi, A.N., Shpigun, O.A., Rodin, I.A., 2018. J. Anal. Chem. 73, 1317–1322.
Bétard, A., Fischer, R.A., 2012. Chem. Rev. 112, 1055–1083.
Bian, R., Wang, T., Zhang, L., Li, L., Wang, C., 2015. Biomater. Sci. 3, 1270–1278.
Chen, R., Zhang, J., Wang, Y., Chen, X., Zapien, J.A., Lee, C.S., 2015. Nanoscale 7, 17299–17305.
Chung, H.J., Lim, S., Kim, I.S., Bu, Y., Kim, H., Kim, D.H., Yoo, H.H., 2012. Bull. Korean Chem. Soc. 33, 177–182.
Feng, L., Liu, M., Liu, H., Fan, C., Cai, Y., Chen, L., Zhao, M., Chu, S., Wang, H., 2018. ACS Appl. Mater. Interfaces 10, 23647–23656.
Fu, X., Li, H., Lv, R., Hong, D., Yang, B., Gu, W., Liu, X., 2018a. J. Solid State Chem. 264, 35–41.
Fu, Y., Jin, H., Bu, X., Gui, R., 2018b. J. Agric. Food Chem. 66, 9819–9827.
Gao, J., Wang, C., Tan, H., 2017. J. Mater. Chem. B 5, 9175–9182.
Gao, Q., Xu, S., Guo, C., Chen, Y., Wang, L., 2018. ACS Appl. Mater. Interfaces 10, 16059–16065.
Ge, X., Xia, Z., Guo, S., 2019. Adv. Funct. Mater. 29, 1900318.
Gu, W., Pei, X., Cheng, Y., Zhang, C., Zhang, J., Yan, Y., Ding, C., Xian, Y., 2017a. ACS Sens. 2, 576–582.
Gu, W., Yan, Y., Pei, X., Zhang, C., Ding, C., Xian, Y., 2017b. Sens. Actuators B Chem. 250, 601–607.

Gu, X., He, H., Wang, C.Z., Gao, Y., Zhang, H., Hong, J., Du, S., Chen, L., Yuan, C.S., 2015. RSC Adv. 5, 41377–41384.
Gui, R., Jin, H., Bu, X., Fu, Y., Wang, Z., Liu, Q., 2019. Coord. Chem. Rev. 383, 82–103.
Gui, R., Jin, H., Wang, Z., Li, J., 2018. Chem. Soc. Rev. 47, 6795–6823.
Guo, L.T., Wang, S.Q., Su, J., Xu, L.X., Ji, Z.Y., Zhang, R.Y., Zhao, Q.W., Ma, Z.Q., Deng, X.Y., Ma, S.P., 2019. J. Neuroinflammation 16, 95.
He, X.W., Yu, D., Li, W.L., Zheng, Z., Lv, C.L., Li, C., Liu, P., Xu, C.Q., Hu, X.F., Jin, X.P., 2016. Biomed. Pharmacother. 83, 257–264.
Hu, J., Ji, Y., Mo, Z., Li, N., Xu, Q., Li, Y., Xu, H., Chen, D., Lu, J., 2019. J. Mater. Chem. 7, 4408–4414.
Hu, W., Zhang, W., Wang, M., Feng, F., 2018a. J. Electron. Mater. 47, 1151–1157.
Hu, X., Liu, X., Zhang, X., Chai, H., Huang, Y., 2018b. Biosens. Bioelectron. 105, 65–70.
Huang, X., Song, J., Yung, B.C., Huang, X., Xiong, Y., Chen, X., 2018. Chem. Soc. Rev. 47, 2873–2920.
Jalili, R., Khataee, A., Rashidi, M.R., Luque, R., 2019. Sens. Actuators B Chem. 297, 126775.
Jiang, X., Jin, H., Sun, Y., Gui, R., 2019. Microchim. Acta 186, 580.
Jin, H., Gui, R., Yu, J., Lv, W., Wang, Z., 2017. Biosens. Bioelectron. 91, 523–537.
Jin, J., Zheng, Y., Huang, S.Z., Sun, P.P., Srikanth, N., Kong, L.B., Yan, Q., Zhou, K., 2019a. J. Mater. Chem. 7, 783–790.
Jin, X., Liu, M.Y., Zhang, D.F., Zhong, X., Du, K., Qian, P., Yao, W.F., Gao, H., Wei, M.J., 2019b. CNS Neurosci. Ther. 25, 575–590.
Kim, D.H., Kim, J.M., Lee, E.K., Choi, Y.J., Kim, C.H., Choi, J.S., Kim, N.D., Yu, B.P., Chung, H.Y., 2012. J. Nutr. Biochem. 23, 1277–1284.
Lai, Z., 2018. Curr. Opin. Chem. Eng. 20, 78–85.
Lee, M., Park, Y.H., Kang, E.B., Chae, A., Choi, Y., Jo, S., Kim, Y.J., Park, S.J., Min, B., An, T.K., et al., 2017. ACS Omega 2, 7096–7105.
Lee, M.H., Kim, J.S., Sessler, J.L., 2015a. Chem. Soc. Rev. 44, 4185–4191.
Lee, W., Ku, S.K., Bae, J.S., 2015b. Arch Pharm. Res. (Seoul) 38, 893–903.
Li, J., Wang, H., Shi, X., Zhao, L., Lv, T., Yuan, Q., Hao, W., Zhu, J., 2019. J. Ethnopharmacol. 235, 155–163.
Li, Y., Hu, Y., Zhao, Y., Shi, G., Deng, L., Hou, Y., Qu, L., 2011. Adv. Mater. 23, 776–780.
Lin, L., Xu, Y., Zhang, S., Ross, I.M., Ong, A.C.M., Allwood, D.A., 2014. Small 10, 60–65.
Liu, J., Liu, T., Du, P., Zhang, L., Lei, J., 2019a. Angew. Chem. Int. Ed. 58, 7808–7812.
Liu, Y., Gong, C.S., Lin, L., Zhou, Z., Liu, Y., Yang, Z., Shen, Z., Yu, G., Wang, Z., Wang, S., et al., 2019b. Theranostics 9, 2791–2799.
Liu, Z., Zhang, A., Guo, Y., Dong, C., 2014. Biosens. Bioelectron. 58, 242–248.
Long, L., Niu, X., Yan, K., Zhou, G., Wang, J., Wu, X., Chu, P.K., 2018. Small 14, 1803132.
Ma, Y., Xu, G., Wei, F., Cen, Y., Ma, Y., Song, Y., Xu, X., Shi, M., Muhammad, S., Hu, Q., 2017. J. Mater. Chem. C 5, 8566–8571.
Meng, X., Hu, L., Li, W., 2019. N-S Arch. Pharmacol. 392, 1421–1433.
Ren, H., Zhang, L., An, J., Wang, T., Li, L., Si, X., He, L., Wu, X., Wang, C., Su, Z., 2014. Chem. Commun. 50, 1000–1002.
Ren, S.H., Liu, S.G., Ling, Y., Li, N.B., Luo, H.Q., 2018. Spectrochim. Acta 201, 112–118.
Sammi, H., Kukkar, D., Singh, J., Kukkar, P., Kaur, R., Kaur, H., Rawat, M., Singh, G., Kim, K.H., 2018. Sens. Actuators B Chem. 255, 3047–3056.
Shen, J., Cheng, J., Zhu, S., Zhao, J., Ye, Q., Xu, Y., Dong, H., Zheng, X., 2019. Int. Immunopharmacol. 73, 193–200.
Sheng, K., Wang, L., Li, H., Zou, L., Ye, B., 2017. Talanta 164, 249–256.
Sithisarn, P., Rojsanga, P., Sithisarn, P., 2019. Molecules 24, 1937.
Stengl, V., Henych, J., 2013. Nanoscale 5, 3387–3394.
Sun, Y., Jiang, X., Jin, H., Gui, R., 2019. Anal. Chim. Acta 1083, 101–109.
Tong, L., Wan, M., Zhang, L., Zhu, Y., Sun, H., Bi, K., 2012. J. Pharm. Biomed. Anal. 70, 6–12.
Wang, H., 2010. Food Drug 12, 347–350.
Wang, K., Li, N., Zhang, J., Zhang, Z., Dang, F., 2017. Biosens. Bioelectron. 87, 339–344.
Wang, L., Xu, Q., Xu, J., Weng, J., 2016. RSC Adv. 6, 69033–69039.
Wang, M., Liang, Y., Liu, Y., Ren, G., Zhang, Z., Wu, S., Shen, J., 2018a. Analyst 143, 5822–5833.
Wang, X., Li, P., Liu, Z., He, Y., 2013. Colloids Surf., A 421, 118–124, 2013.
Wang, Y., Cheng, J., Liu, X., Ding, F., Zou, P., Wang, X., Zhao, Q., Rao, H., 2018b. ACS Sustain. Chem. Eng. 6, 16847–16858.
Wei, Y., Pi, C., Yang, G., Xiong, X., Lan, Y., Yang, H., Zhou, Y., Ye, Y., Zou, Y., Zheng, W., Zhao, L., 2016. Molecules 21, 444.
Wu, P., Hou, X., Xu, J.J., Chen, H.Y., 2016. Nanoscale 8, 8427–8442.
Wu, Y., Wang, F., Fan, L., Zhang, W., Wang, T., Du, Y., Bai, X., 2018. Biomed. Pharmacother. 97, 1673–1679.
Xiao, D., Yang, D., Chen, Y., Liu, W., 2019. Biosci. Rep. 39, BSR20181692.
Xie, Z., Lu, W., Yang, L., Li, G., Ye, B., 2017. Talanta 170, 358–368.
Xiong, H., Wang, W., Liang, J., Wen, W., Zhang, X., Wang, S., 2016. Biosens. Bioelectron. 86, 164–168.
Xu, L., Fang, G., Liu, J., Pan, M., Wang, R., Wang, S., 2016. J. Mater. Chem. 4, 15880–15887.
Ye, J.W., Zhou, H.L., Liu, S.Y., Cheng, X.N., Lin, R.B., Qj, X.L., Zhang, J.P., Chen, X.M., 2015. Chem. Mater. 27, 8255–8260.
Yue, Q., Hu, Y., Tao, L., Zhang, B., Liu, C., Wang, Y., Chen, C., Zhao, J., Li, C.Z., 2019. Microchim. Acta 186, 640.
Zhang, H., Wang, T., Qiu, Y., Fu, F., Yu, Y., 2016a. J. Electroanal. Chem. 775, 286–291.
Zhang, H.M., Yang, H., Zheng, H.Z., 2016b. Chin. J. N. Drugs Clin. Remedies 35, 704–708.
Zhang, X., Xie, H., Liu, Z., Tan, C., Luo, Z., Li, H., Lin, J., Sun, L., Chen, W., Xu, Z., Xie, L., Huang, W., Zhang, H., 2015. Angew. Chem. Int. Ed. 54, 3653–3657.
Zhong, G., Liu, D., Zhang, J., 2018. J. Mater. Chem. 6, 1887–1899.